Transient current in a quantum dot subject to a change in coupling to its leads

Transient current in a quantum dot subject to a change in coupling to its leads

A F Izmaylov[1], A Goker[2], B A Friedman[3] and P Nordlander[2]

[1] Department of Chemistry, Rice University, Houston, TX 77005-1892, USA
[2] Department of Physics and Department of Electrical and Computer Engineering, Rice Quantum Institute, Rice University, Houston, TX 77251-1892, USA
[3] Department of Physics, Sam Houston State University, Huntsville, TX 77341, USA

E-mail: nordland@rice.edu

Abstract
The time-dependent non-crossing approximation is used to calculate the transient currents through a quantum dot in the Kondo regime subject to a sudden change in its coupling to the leads. The currents are found to display transient non-universal behaviour immediately after the perturbation and then to follow a slow universal increase toward equilibrium. The timescales for the approach to equilibrium are shown to be the same as those recently identified in a study of transient currents in a quantum dot subject to a sudden change in the energy of the dot level (Plihal *et al* 2005 *Phys. Rev.* B **71** 165321). We present improved numerical algorithms which enable relatively fast calculation of the transient response of quantum dots to sudden perturbations.

(Some figures in this article are in colour only in the electronic version)

1. Introduction

The understanding of the non-equilibrium real-time evolution of quantum many-body systems is much less advanced than the understanding of systems in equilibrium. Non-equilibrium effects are responsible for important phenomena such as dissipation and decoherence in electron transport through nanodevices. Quantum dots and qubits fall into this category, where a mesoscopic device interacts with a fermionic or bosonic bath. Advances in the nanofabrication of quantum dots have made it possible to study non-equilibrium transport phenomena in quantum dots in a controlled manner. Recently, Elzerman *et al* have emphasized the practical importance of real-time dynamics in quantum dots for quantum computation [1]. This type of system constitutes an ideal platform to study the Kondo effect out of equilibrium, since one can electrically tune the parameters of quantum dots.

The Kondo effect was first discovered in bulk metals with magnetic impurities providing localized unpaired spins [2] and was observed later in semiconducting quantum dots [3–5]. It is a many-body effect in which conduction electrons in the vicinity of a spin impurity

screen the spin to form a collective entangled ground state at low temperatures [6]. The most evident manifestation of Kondo physics in quantum dots occurs when an odd number of electrons is confined within the dot. The resulting net spin is coupled to the fermionic bath at low temperatures and a sharp peak forms at the Fermi level in the dot density of states. The consequence of this Kondo peak is a large enhancement of the dot's conductance. This enhancement strongly depends on temperature, bias, and magnetic field [7–11].

Several theoretical groups have considered the effects of time-dependent ac perturbations of the bias and gate potentials on the transport through quantum dots in the Kondo regime [12–18]. Kondo sidebands induced by ac perturbations of the dot have recently been observed in transport experiments on a single dot [19].

The application of abrupt perturbations by step-like switching of the gate potential or bias [20–26] can determine the intrinsic timescales associated with the Kondo problem more precisely than ac modulation. Three timescales have recently been identified in the transient currents after a sudden shift of the dot level in a quantum dot coupled to two leads [20, 21]. The fastest (and trivial) timescale corresponds to charge relaxation and is associated with the reshaping of the dot level due to its interaction with the conduction bands of the leads. This is a non-universal non-Kondo timescale and is inversely proportional to the life-time broadening of the dot level. The second timescale is the time it takes for the conductance of the dot to reach within a few per cent of its equilibrium value. The third and longest timescale, which is only present for finite bias across the dot, is the time it takes for the split Kondo peak (SKP) oscillations caused by the interference of the Kondo resonances on each lead to dampen out.

In this paper, we analyse the conductance of a quantum dot subject to a sudden change of coupling to its leads. We develop an efficient implementation of our numerical approach for the solution of the time-dependent non-crossing approximation (NCA) equations [27]. This numerical improvement allows us to investigate the time-dependent response of quantum dots for lower temperatures and smaller biases and with greater speed than in our previous applications [20]. A comparison of the transient currents following a sudden shift in the coupling of the dot level to its leads with the transient currents following a sudden shift of the dot level into the same state shows that the response is almost identical. The two longer timescales are found to be the same.

2. Method

The quantum dot is modelled by a single spin degenerate level of energy $\varepsilon_{\mathrm{dot}}$ coupled to leads through tunnel barriers. This system is described by the Anderson Hamiltonian

$$H(t) = \sum_{\sigma} \varepsilon_{\mathrm{dot}}(t) n_{\sigma} + \sum_{k\sigma} \varepsilon_k n_{k\sigma} + \tfrac{1}{2} \sum U_{\sigma,\sigma'} n_{\sigma} n_{\sigma'} + \sum_{\sigma k} \left[V_k(t) c_{k\sigma}^{\dagger} c_{\sigma} + \mathrm{H.c.} \right], \tag{1}$$

where $c_{\sigma}^{\dagger}$ (c_{σ}) and $c_{k\sigma}^{\dagger}$ ($c_{k\sigma}$) create (annihilate) an electron of spin σ in the dot level and in the leads, respectively; n_{σ} and $n_{k\sigma}$ are the corresponding number operators; and V_k is a hopping amplitude. The Coulomb repulsion energy U is assumed to be sufficiently large so that double occupancy of the dot level is prohibited. In the following, we will use atomic units with $\hbar = k_{\mathrm{B}} = e = 1$.

The spectral function of the dot level has two features when the dot level $\varepsilon_{\mathrm{dot}}$ is well below the Fermi level ε_{F}. First, there is a broad Fano-like resonance around the dot level energy due to the tunnelling of electrons between the dot and the leads. The half-width of this resonance is

$$\Gamma(\varepsilon, t) = 2\pi \sum_{k} |V_k(t)|^2 \delta(\varepsilon - \varepsilon_k), \tag{2}$$

provided that charge relaxation is much faster than the timescale for the change of $V(t)$. Second, there is a sharp temperature-sensitive resonance at the Fermi level (the Kondo peak), characterized by a low energy scale T_K (the Kondo temperature):

$$T_K = \left(\frac{D\Gamma}{4}\right)^{1/2} \exp\left(-\frac{\pi|\varepsilon_{dot}|}{\Gamma}\right),$$ (3)

where D is a high-energy cutoff equal to the half bandwidth modelled by a symmetric flat band, and Γ corresponds to $\varepsilon = \varepsilon_F$. Here we use a symmetric parabolic band of half bandwidth $D = 9\Gamma$ [27].

The currents through the dots are calculated directly from the current operator,

$$I_{in}(t) = i \sum_{k\sigma} V_k(t)\langle c_{k\sigma}^\dagger(t) c_\sigma(t)\rangle + \text{c.c.},$$ (4)

where $\langle c_{k\sigma}^\dagger(t) c_\sigma(t)\rangle$ is the Keldysh propagator, which can be evaluated from the Kadanoff–Baym time-dependent Green functions [27]. $I_{in}(t)$ can be divided into contributions $I_{left}(t)$ and $I_{right}(t)$ by restricting the k summations to the appropriate lead. The transport current is given by $I(t) = [I_{left}(t) - I_{right}(t)]/2$.

In our method, the Green functions are solutions of the real-time coupled integro-differential Dyson equations with non-crossing approximation (NCA) for the self-energy. In the numerical algorithm [27] the Green functions $G(t, t')$ are discretized on a uniform time grid represented by matrices $G(m, n)$ of size $N \times N$. To model time-dependent phenomena, these matrices are propagated in time. In each propagation step, N matrix elements must be updated by integrals of the values of the Green functions and the self-energies over N previous time steps. Each step of the matrix propagation thus scales quadratically with the matrix size, and the computational scaling of the algorithm [27] is $O(MN^2)$, where M is the number of propagation steps. For low temperatures, the size of the matrices must be taken to be very large, because of the importance of long-timescale correlations. The resulting computational expense was one of the main obstacles preventing a thorough investigation of transient transport in the temperature range below T_K. In the current paper, we use an improved numerical method for the evaluation of the integrals in the coupled Dyson equations. The new algorithm employs a multigrid approach where, in addition to a fine grid (with grid size δ), we also use a coarse grid (with grid size $\Delta = \delta N_g$). The use of a multi-grid allows us to reduce substantially the computational effort required for evaluation of the integrals. The computational scaling of the new algorithm, which is described in the appendix, is $O(MN^2/N_g)$.

Throughout this paper, we study the same two systems which were investigated by Plihal *et al* [20]: *system one* (S1) with $\varepsilon_{dot} = -2\Gamma$ and $T_K = 0.0022\Gamma$ and *system two* (S2) with $\varepsilon_{dot} = -2.225\Gamma$ and $T_K = 0.0011\Gamma$. The dot levels ε_{dot} are kept fixed. The dot–lead tunnelling rates are abruptly switched at $t = 0$ from a small Γ_0 (0.003 68 au), for which the current is small, and $T_K \ll T$, to Γ (0.0092 au) for which the Kondo effect arises.
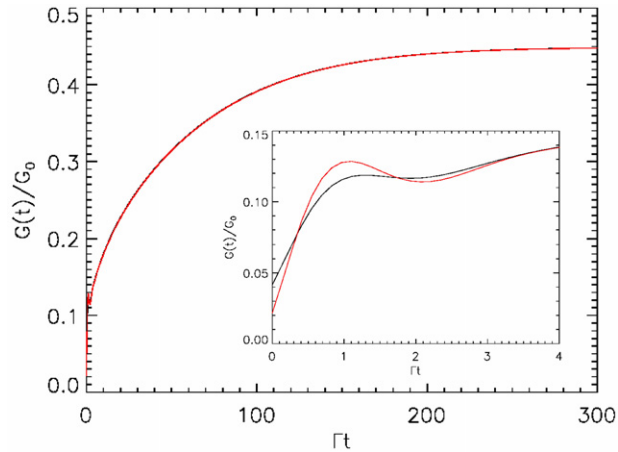
In figure 1, we show how the calculated instantaneous conductance depends on grid ratio N_g (see appendix) for system S2 for two different temperatures. In the present paper, we use a fine grid spacing of $\delta = 15$ au, which is adequate for both S1 and S2 [27]. As we see in the magnified panels, we achieve a good convergence as we reduce the grid ratio. The data presented below was calculated using a grid ratio of $N_g = 20$.

3. Results

In figure 2, we compare the instantaneous conductance resulting from a sudden change in Γ with the instantaneous conductance resulting from a change in the energy of the dot level for
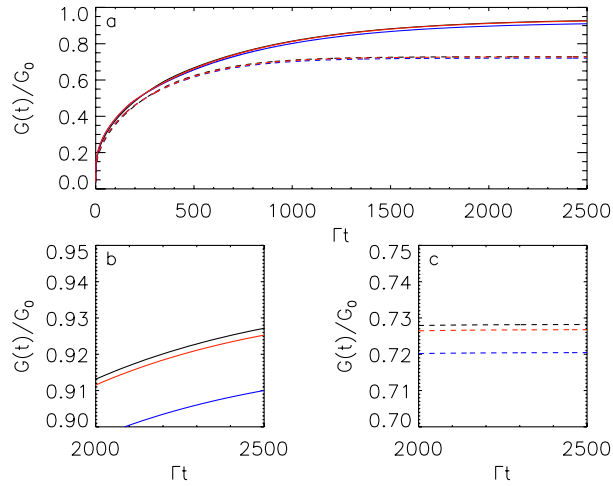
Figure 1. Convergence of the calculated time-dependent conductance curves for S2 as a function of grid ratio N_g with fixed fine grid spacing $\delta = 15$ au. Solid curves are for $T = 0.0005\Gamma$ and the dashed curves are for $T = 0.0015\Gamma$. Black, red and blue curves (top to bottom) correspond to grid ratio N_g of 20, 40 and 80, respectively. Panels (b) and (c) magnify the long-time part of panel (a).

Figure 2. Comparison of instantaneous conductance for the cases of changing dot–lead coupling constant and the energy of the dot level. We show the rise of the conductance in the final state for S1. The calculation was carried out at $T = 0.005\Gamma$ to make both timescales visible. The red curve corresponds to changing the dot level abruptly and the black curve is for changing the dot–lead tunnelling constant. In the inset, we show the initial non-universal response on a magnified scale.

system S1 at a temperature above T_K for infinitesimal bias. The figure clearly illustrates that the approach to steady state occurs on the same timescale for both dot level and dot coupling change. The curves only differ in the non-universal regime for $t < 4\Gamma$. The initial state in both calculations was chosen to have the same ratio $\varepsilon_{dot}/\Gamma_0$. If different initial states are chosen, the differences in the conductances persist to slightly longer times, but the asymptotic timescale (rise time of the conductance) would remain the same. We can thus conclude that the timescale for approach to equilibrium is determined by the electronic structure of the final state.
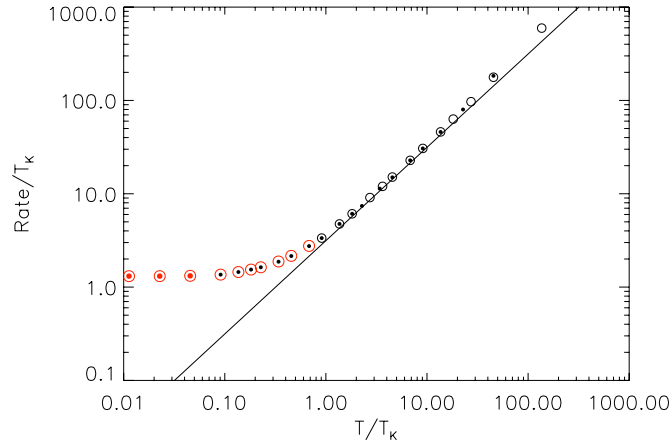
Figure 3. Rise rate, which is defined as the time it takes for instantaneous conductance to reach 99% of its final value, for S1 and S2 versus temperature T for infinitesimal bias. The solid dots are for S1 and the open circles are for S2. Small (black) circles and small dots represent the data obtained previously [20]. Large (red) circles and large dots correspond to the data taken with the new numerical scheme. The straight line has a slope of π and passes through the origin.

3.1. Initial non-universal conductance

Figure 2 shows well-defined oscillations in the non-universal timescale reminiscent of Rabi oscillations [20, 28]. We observe these oscillations for all temperatures considered. These fast oscillations can be attributed to the charge relaxation, because the spin flips that give rise to the Kondo resonance are absent in the non-universal timescale. This implies that one can neglect the spin-dependent terms in equation (1) and solve the remaining part. Both the amplitude and frequency of these initial oscillations can be reproduced using the master equation approach developed previously for the spinless Anderson model in the wide band limit [29].

3.2. Risetime for zero bias

Our new numerical scheme allows us to investigate universality and instantaneous conductances for lower temperatures than was possible previously [20]. In figure 3, we show the calculated rise rates for the approach to equilibrium conductance for S1 and S2. The procedure that we follow to extract these rates is identical to the one used previously [20] and the figure includes the results obtained there for consistency. The solid line is the analytical result for the rise rate [20]. It is clear from these results that the rise rate scales with T_K. This scaling would be preserved in an exact calculation, because it arises from a logarithmic re-summation of perturbation theory, which is included in the NCA and implicit in the exact calculation [17, 30]. Another important conclusion is that the rise rate saturates to a value just above T_K after T/T_K gets smaller than about 0.1.

In figure 4, we plot the final steady-state conductances alongside with the exact asymptotic curve for large $\ln(T/T_K)$ [31] scaled by 4/3 to correct for the NCA error. We present the results obtained previously [20], together with those of the new numerical scheme for lower temperatures. The new scheme allows us to study temperatures as low as $T = 0.1T_K$. The results in figure 4 demonstrate that universality is preserved for temperatures down to a fraction of T_K. Our conductance results for temperatures lower than $T/T_K = 0.1$ in figure 4 exceed the unitarity limit and thus they are not shown. This is a well-known deficiency of NCA, as has been shown in several studies [30].
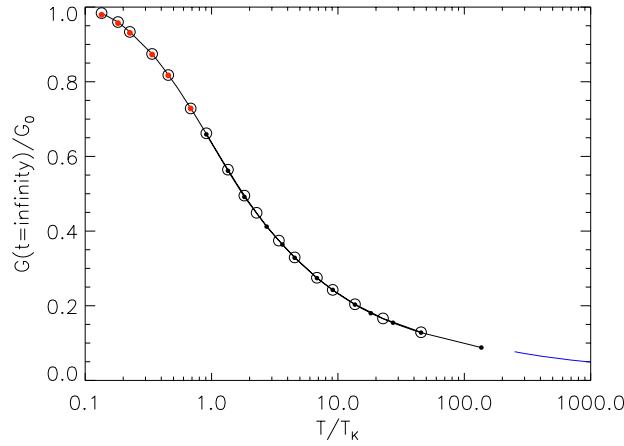
Figure 4. The large-time limit of $G(t)/G_0$ versus temperature for S1 and S2. These are the final steady-state conductance values for infinitesimal bias. Open circles correspond to S1 and solid dots are for S2. Black circles and small dots correspond to the data obtained previously [20] and large (red) dots represent the data taken with the new numerical scheme. The disconnected (blue) line is the large-T asymptote scaled by 4/3.
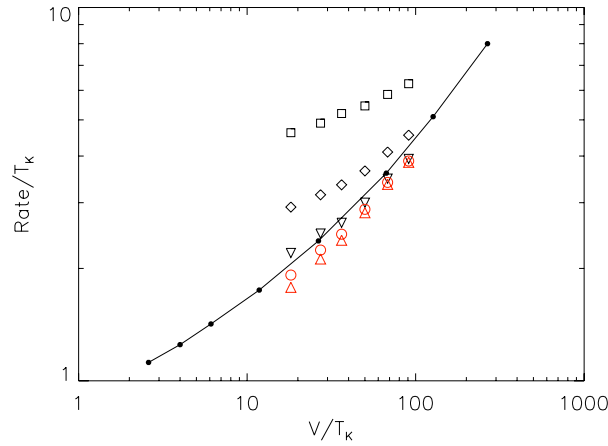
3.3. SKP oscillations

Finally, we would like to discuss the instantaneous conductance at finite bias. For finite bias, two Kondo resonances that correspond to each lead's Fermi level form and broaden compared to the infinitesimal bias situation [28, 32]. When the quantum dot is subject to a sudden change in the dot level, quantum beating between the two Kondo resonances can give rise to an oscillatory conductance, i.e. SKP oscillations. These oscillations can persist to long times and their period is proportional to the bias [20]. The application of a sudden change in the coupling between the dot level and the leads gives rise to the same SKP oscillations as for a sudden change of the dot level.

In figure 5, we show the instantaneous conductance for S1 when the coupling to the leads is changed for a variety of biases. As the bias increases, the frequency of the SKP oscillations increases. The final steady-state value of the conductance decreases because of the suppression of the Kondo resonances for finite bias. We also plot the instantaneous conductance for the largest bias on a magnified scale, where the SKP oscillations and their damping become clearly visible.

Figure 5 clearly illustrates that the SKP oscillations persist to long times. The previous finite temperature study on the bias dependence of the decay rate of the SKP oscillations left open the question whether the numerically observed SKP decay rate was equal to the 2γ rate identified by Rosch *et al* for zero temperature [30]. Using our new numerical scheme, we are able to extend our NCA approach to lower temperatures where a comparison between finite and zero temperatures becomes more meaningful. In figure 6, we plot the calculated SKP decay rates as a function of bias for two new low temperatures along with the data obtained previously. We also show the zero-temperature analytical decoherence rates γ, obtained from the perturbative renormalization group [30]. The figure clearly shows that the calculated decay rates of SKP oscillations saturate as the temperature approaches zero. We find that half the decay rates obtained from our NCA calculations correspond to roughly 2γ. It is somewhat surprising that the NCA results agree quantitatively with those of the analytical method, since the latter includes a vertex correction which is absent in NCA. We cannot rule out that the small deviation between our calculated decay rates for the lowest temperatures and bias is an NCA error.
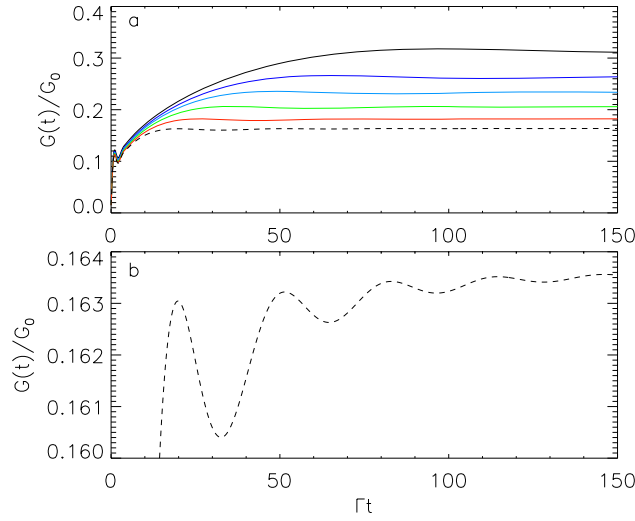
Figure 5. Instantaneous conductance of S1 for finite bias (V) at $T = 0.17T_K$ right after the coupling to the leads is switched. Black, dark blue, light blue, green, red and dashed black curves (top to bottom) correspond to $V = 0.04\Gamma, 0.06\Gamma, 0.08\Gamma, 0.11\Gamma, 0.15\Gamma$ and 0.2Γ, respectively, in panel (a). In panel (b), we show the instantaneous conductance for $V = 0.2\Gamma$ on a magnified scale.

Figure 6. Decay of SKP oscillations versus bias V for S1. Solid circles represent the analytical calculations of 2γ at zero temperature [30]. Black squares, diamonds and downwards triangles are previous results [20] and correspond to $T = 1.4T_K, 0.69T_K$ and $0.34T_K$, respectively. Red open circles and upwards triangles are the new data obtained for $T = 0.17T_K$ and $0.08T_K$.

4. Conclusion

In this paper, we have analysed the transient conductance of a quantum dot when the dot–lead tunnelling rate is suddenly switched to a value where the Kondo effect is present. Our results show that the transient currents induced by changing the coupling to the leads are almost identical to the currents induced by changing the energy of the dot level. Using a new numerical scheme, we are able to extend our approach to low temperatures. The decay rates of the SKP oscillation were found to saturate for low temperatures to values very close to two times the

decoherence rate obtained from the perturbative renormalization group studies. We hope that these predictions will motivate further experimental and theoretical studies.

Acknowledgments

Appendix. Details of the numerical implementation

In this appendix, we present an improved version of the algorithm for numerical solution of the Dyson equations introduced in [27]. Here we will follow the notation of Shao *et al* [27]. Let us start from a consideration of retarded Green's functions. The Dyson equations for $g_\sigma(t, t')$ and $b(t, t')$ with $t \geqslant t'$ are

$$\frac{\partial}{\partial t} g_\sigma(t, t') = -\int_{t'}^{t} d\bar{t} \, \tilde{K}_\sigma^>(t, \bar{t}) b(t, \bar{t}) g_\sigma(\bar{t}, t'), \tag{A.1}$$

$$\frac{\partial}{\partial t} b(t, t') = -\sum_\sigma \int_{t'}^{t} d\bar{t} \, \tilde{K}_\sigma^<(\bar{t}, t) g_\sigma(t, \bar{t}) b(\bar{t}, t'). \tag{A.2}$$

For $t < t'$, the $g_\sigma(t, t')$ and $b(t, t')$ functions can be determined by

$$g_\sigma(t', t) = g_\sigma^*(t, t'),$$
$$b(t', t) = b^*(t, t'). \tag{A.3}$$

We can represent the Green's functions as

$$g_\sigma(t, t') = g_\sigma^f(t, t') e^{i\omega_g(t-t')},$$
$$b(t, t') = b^f(t, t') e^{i\omega_b(t-t')}, \tag{A.4}$$

where $e^{i\omega_g(t-t')}$ and $e^{i\omega_b(t-t')}$ are the oscillatory 'carrier' parts and $g_\sigma^f(t, t')$ and $b^f(t, t')$ denote smooth, envelope-like modulating functions (see figure A.1). Figure (A.1) shows that, after a certain time difference $t - t'$, the Green's functions $g_\sigma^f(t, t')$ and $b^f(t, t')$ behave almost linearly. We will refer to this time difference as Δt_{lin}. By substituting equations (A.4) in equations (A.1) and (A.2), one can obtain

$$\frac{\partial}{\partial t} \left[g_\sigma^f(t, t') e^{i\omega_g(t-t')} \right] = -\int_{t'}^{t} d\bar{t} \, \tilde{K}_\sigma^>(t, \bar{t}) e^{i\omega_b(t-\bar{t})} e^{i\omega_g(\bar{t}-t')} b^f(t, \bar{t}) g_\sigma^f(\bar{t}, t'), \tag{A.5}$$

$$\frac{\partial}{\partial t} \left[b^f(t, t') e^{i\omega_b(t-t')} \right] = -\sum_\sigma \int_{t'}^{t} d\bar{t} \, \tilde{K}_\sigma^<(\bar{t}, t) e^{i\omega_g(t-\bar{t})} e^{i\omega_b(\bar{t}-t')} g_\sigma^f(t, \bar{t}) b^f(\bar{t}, t'). \tag{A.6}$$

In steady state, both kernels depend only on the time difference rather than on individual values of t and $\bar{t}$. The kernels can be combined with the oscillatory parts in the following manner:

$$\tilde{K}_\sigma^>(t, \bar{t}) e^{i\omega_b(t-\bar{t})} e^{i\omega_g(\bar{t}-t')} = \tilde{K}_\sigma^>(t, \bar{t}) e^{i(\omega_b-\omega_g)(t-\bar{t})} e^{i\omega_g(t-t')}$$
$$= \tilde{K}_{\sigma\omega}^>(t-\bar{t}) e^{i\omega_g(t-t')}, \tag{A.7}$$

and

$$\tilde{K}_\sigma^<(\bar{t}, t) e^{i\omega_g(t-\bar{t})} e^{i\omega_b(\bar{t}-t')} = \tilde{K}_\sigma^<(\bar{t}, t) e^{i(\omega_g-\omega_b)(t-\bar{t})} e^{i\omega_b(t-t')}$$
$$= \tilde{K}_{\sigma\omega}^<(\bar{t}-t) e^{i\omega_b(t-t')}. \tag{A.8}$$

Let us illustrate our discretization scheme on the integral part of equation (A.6). First we split the $[t', t]$ range into pieces:
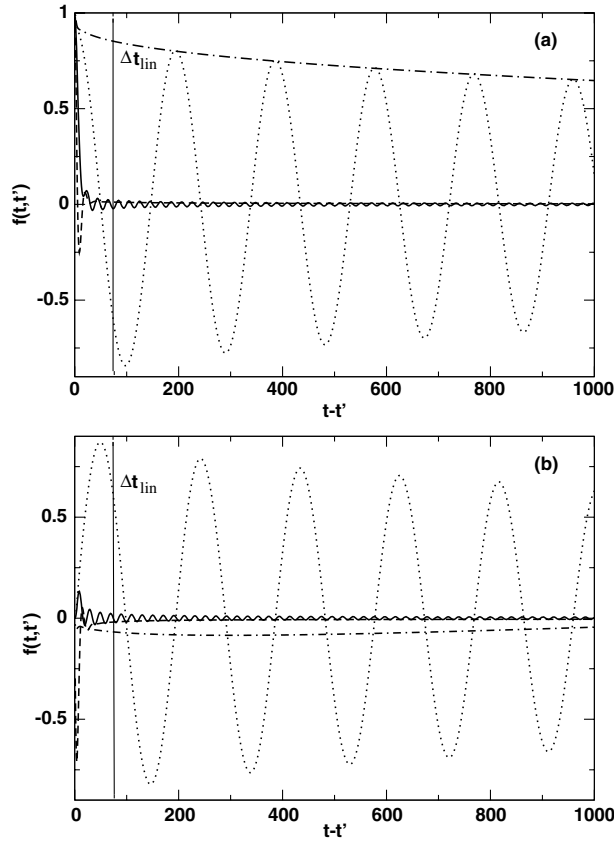
Figure A.1. Real (a) and imaginary (b) parts of retarded Green's functions $g_\sigma(t, t')$ dotted (black), $g_\sigma^f(t, t')$ dash–dotted (red), $b(t, t')$ solid (blue), and $b^f(t, t')$ dashed (green) for S1 with $N = 1000$, and fixed t.

$$\int_{t'}^t d\bar{t}\, \tilde{K}_{\sigma\omega}^<(\bar{t}, t) g_\sigma^f(t, \bar{t}) b^f(\bar{t}, t')$$

$$= \left[\int_{t'}^{t'+\Delta t_{\text{lin}}} + \int_{t-\Delta t_{\text{lin}}}^t + \int_{t'+\Delta t_{\text{lin}}}^{t-\Delta t_{\text{lin}}} \right] d\bar{t}\, \tilde{K}_{\sigma\omega}^<(\bar{t}, t) g_\sigma^f(t, \bar{t}) b^f(\bar{t}, t'). \tag{A.9}$$

We will refer to the intervals $[(t - \bar{t}) < \Delta t_{\text{lin}}$ or $(\bar{t} - t') < \Delta t_{\text{lin}}]$ and $[(t - \bar{t}) > \Delta t_{\text{lin}}$ and $(\bar{t} - t') > \Delta t_{\text{lin}}]$ as $\bar{\mathcal{L}}$ and $\mathcal{L}$, respectively. For the $\bar{\mathcal{L}}$ interval, we use trapezoidal quadrature on the fine grid (grid size δ):

$$\int_{t'}^{t'+\Delta t_{\text{lin}}} d\bar{t}\, \tilde{K}_{\sigma\omega}^<(\bar{t}, t) g_\sigma^f(t, \bar{t}) b^f(\bar{t}, t') = \delta \sum_{j=n}^k c_j \tilde{K}_{\sigma\omega}^<(m, j) b^f(m, j) g_\sigma^f(j, n). \tag{A.10}$$

Here we use integers j, n, k, and m for the time arguments, $c_j = 1/2$ for $j = n, k$, and $c_j = 1$ in all other cases. In the $\mathcal{L}$ interval, we employ the following decomposition:

$$\int_{t'+\Delta t_{\text{lin}}}^{t-\Delta t_{\text{lin}}} d\bar{t}\, \tilde{K}_{\sigma\omega}^<(\bar{t}, t) g_\sigma^f(t, \bar{t}) b^f(\bar{t}, t') = \sum_i \int_{\Delta_i} d\bar{t} \tilde{K}_{\sigma\omega}^<(\bar{t}, t) g_\sigma^f(t, \bar{t}) b^f(\bar{t}, t')$$

$$= \sum_i g_\sigma^f(t, \bar{\xi}_i) b^f(\bar{\xi}_i, t') \int_{\Delta_i} d\bar{t}\, \tilde{K}_{\sigma\omega}^<(\bar{t}, t), \tag{A.11}$$

where $\Delta_i = [\bar{t}_i, \bar{t}_{i+1}]$ is the ith coarse grid interval and $\bar{\xi}_i \in \Delta_i$. We assume that

$$g_\sigma^f(t, \bar{\xi}_i) b^f(\bar{\xi}_i, t') \cong \tfrac{1}{2} \left[g_\sigma^f(t, \bar{t}_i) b^f(\bar{t}_i, t') + g_\sigma^f(t, \bar{t}_{i+1}) b^f(\bar{t}_{i+1}, t') \right], \tag{A.12}$$

because of the linear character of the Green's functions in the $\mathcal{L}$ interval. To obtain an accurate estimate for the oscillatory kernel integration in equation (A.11), we use the fine grid and Simpson's quadrature:

$$\int_{\Delta_i} \tilde{K}_{\sigma\omega}^<(\bar{t}, t) \, \mathrm{d}\bar{t} \cong \delta \sum_j w_j \tilde{K}_{\sigma\omega}^<(\bar{t}_j - t) = \tilde{K}_{\sigma P}^<(\bar{t}_i, t), \tag{A.13}$$

where w_j are the weights. Due to the translational invariance of the kernels, one can pre-compute $\tilde{K}_{\sigma P}^<(\bar{t}_i, t)$ values and keep them in the core memory during the calculation.

In the differential part, we use an analytic expression for the oscillatory part and finite differences on the fine grid for the non-periodic part:

$$\frac{\partial}{\partial t} \left[g_\sigma^f(t, t') \mathrm{e}^{\mathrm{i}\omega_g(t-t')} \right] \cong \mathrm{e}^{\mathrm{i}\omega_g(t-t')} \left[\mathrm{i}\omega_g g_\sigma^f(t, t') + \frac{g_\sigma^f(t, t') - g_\sigma^f(t - \delta, t')}{\delta} \right]. \tag{A.14}$$

The discretized version of equations (A.5) and (A.6) can be written as

$$\left(1 + \frac{\mathrm{i}\delta\omega_g}{2} \right) g_\sigma^f(m, n) = \left(1 - \frac{\mathrm{i}\delta\omega_g}{2} \right) g_\sigma^f(m - 1, n) - \frac{1}{2} \left[L_g(m, n) + \bar{L}_g(m, n) \right]$$
$$- \frac{\mathrm{e}^{-\mathrm{i}\delta\omega_g}}{2} \left[L_g(m - 1, n) + \bar{L}_g(m - 1, n) \right], \tag{A.15}$$

and

$$\left(1 + \frac{\mathrm{i}\delta\omega_b}{2} \right) b^f(m, n) = \left(1 - \frac{\mathrm{i}\delta\omega_b}{2} \right) b^f(m - 1, n) - \frac{1}{2} \left[L_b(m, n) + \bar{L}_b(m, n) \right]$$
$$- \frac{\mathrm{e}^{-\mathrm{i}\delta\omega_b}}{2} \left[L_b(m - 1, n) + \bar{L}_b(m - 1, n) \right], \tag{A.16}$$

where

$$\bar{L}_g(m, n) = \delta^2 \left[\sum_{j=n}^{p} c_j \tilde{K}_{\sigma\omega}^>(m, j) b^f(m, j) g_\sigma^f(j, n) + \sum_{j=r}^{m} c_j \tilde{K}_{\sigma\omega}^>(m, j) b^f(m, j) g_\sigma^f(j, n) \right],$$

$$L_g(m, n) = \Delta\delta \sum_{s=p}^{r} c_s \tilde{K}_{\sigma P}^>(m, s) b^f(m, s) g_\sigma^f(s, n), \tag{A.17}$$

$$\bar{L}_b(m, n) = \delta^2 \sum_\sigma \left[\sum_{j=n}^{p} c_j \tilde{K}_{\sigma\omega}^<(m, j) g_\sigma^f(m, j) b^f(j, n) \right.$$
$$\left. + \sum_{j=r}^{m} c_j \tilde{K}_{\sigma\omega}^<(m, j) g_\sigma^f(m, j) b^f(j, n) \right], \tag{A.18}$$

$$L_b(m, n) = \Delta\delta \sum_\sigma \sum_{s=p}^{r} c_s \tilde{K}_{\sigma P}^<(m, s) g_\sigma^f(m, s) b^f(s, n). \tag{A.19}$$

Here we use integers i, j, m, and n to denote time arguments on the fine grid in the $\bar{\mathcal{L}}$ interval. The indices p, q, r refer to time arguments on the coarse grid in the $\mathcal{L}$ interval. The indices p and q appear in the $\bar{\mathcal{L}}$ sums as well, since the fine grid is a subgrid of the coarse grid. Let us denote by $N_g = \Delta/\delta$ the number of fine grid points between two adjacent coarse grid points and by N the number of fine grid points in the Green's function matrix representation. With increasing length of the $[t', t]$ interval, the length of the $\bar{\mathcal{L}}$ interval remains constant,

but the length of the $\mathcal{L}$ interval grows linearly. Therefore, in the large-N limit, the dominant contribution to the computational cost for evaluating equations (A.15) and (A.16) comes from the $\mathcal{L}$ interval and will now scale as $O(N/N_g)$. To evaluate the Green's function matrices, we solve equations (A.15) and (A.16) for all elements in the same order as reported in [27]. The computational scaling of the Green's function matrix construction by the method presented in [27] is $O(N^3)$. The new scheme reduces the scaling down to $O(N^3/N_g)$ by using pre-integration in the $\mathcal{L}$ range without losing accuracy.

In order to obtain good estimates for the frequencies ω_g and ω_b, we use the previous implementation [27] with small Ns and extract the frequencies from the Green's functions. We found that the values of ω_g and ω_b are not sensitive to the size of the Green's function matrix representation.

The same pre-integration scheme can be straightforwardly applied to the 'less than' Green's function equations, although the expressions become more cumbersome than in the retarded case.

To take into account the abrupt change of the dot–lead tunnelling rate or the position of the dot level, we modify equations (A.4) as

$$
\begin{aligned}
g_\sigma(t, t') &= g_\sigma^f(t, t')e^{i\omega_{1g}(t-t')} + \theta(t - t_1)\theta(t' - t_1)g_\sigma^f(t, t')(e^{i\omega_{2g}(t-t')} - e^{i\omega_{1g}(t-t')}), \\
b(t, t') &= b^f(t, t')e^{i\omega_{1b}(t-t')} + \theta(t - t_1)\theta(t' - t_1)b^f(t, t')(e^{i\omega_{2b}(t-t')} - e^{i\omega_{1b}(t-t')}).
\end{aligned}
\tag{A.20}
$$

In equations (A.20), ω_1 and ω_2 correspond to the oscillation frequencies of the first and second state, respectively, and t_1 is the time of the sudden change. One can apply the two-grid scheme for this case as well.

References

[1] Elzerman J M, Hanson R, van Beveren L H W, Witkamp B, Vandersypen L M K and Kouwenhoven L P 2004 *Nature* **430** 431–4
[2] Kondo J 1964 *Prog. Theor. Phys.* **32** 37
[3] Goldhaber-Gordon D, Shtrikman H, Mahalu D, Abusch-Magder D, Meirav U and Kastner M A 1998 *Nature* **391** 156–9
[4] Goldhaber-Gordon D, Gores J, Kastner M A, Shtrikman H, Mahalu D and Meirav U 1998 *Phys. Rev. Lett.* **81** 5225–8
[5] Cronenwett S M, Osterkamp T H and Kouwenhoven L P 1998 *Science* **281** 540–4
[6] Pustilnik M and Glazman L 2004 *J. Phys.: Condens. Matter* **16** R513–37
[7] Ng T K and Lee P A 1988 *Phys. Rev. Lett.* **61** 1768
[8] Glazman L I and Raikh M E 1988 *JETP Lett.* **47** 452
[9] Giuliano D, Naddeo A and Tagliacozzo A 2004 *J. Phys.: Condens. Matter* **16** S1453–83
[10] Hewson A C, Bauer J and Oguri A 2005 *J. Phys.: Condens. Matter* **17** 5413–22
[11] Swirkowicz R, Wilczynski M and Barnas J 2006 *J. Phys.: Condens. Matter* **18** 2291–304
[12] Hettler M H and Schoeller H 1995 *Phys. Rev. Lett.* **74** 4907
[13] Schiller A and Hershfield S 1996 *Phys. Rev. Lett.* **77** 1821
[14] Ng T K 1996 *Phys. Rev. Lett.* **76** 487
[15] Nordlander P, Wingreen N S, Meir Y and Langreth D C 2000 *Phys. Rev.* B **61** 2146–50
[16] Goldin Y and Avishai Y 1998 *Phys. Rev. Lett.* **81** 5394
[17] Kaminsky A, Nazarov Y V and Glazman L I 1999 *Phys. Rev. Lett.* **83** 384
[18] Lu R and Liu Z R 2005 *J. Phys.: Condens. Matter* **17** 5859–67
[19] Kogan A, Amasha S and Kastner M A 2004 *Science* **304** 1293
[20] Plihal M, Langreth D C and Nordlander P 2005 *Phys. Rev.* B **71** 165321
[21] Anders F B and Schiller A 2005 *Phys. Rev. Lett.* **95** 196801
[22] Merino J and Marston J B 2004 *Phys. Rev.* B **69** 115304
[23] Nordlander P, Pustilnik M, Meir Y, Wingreen N S and Langreth D C 1999 *Phys. Rev. Lett.* **83** 808–11
[24] Plihal M, Langreth D C and Nordlander P 2000 *Phys. Rev.* B **61** R13341–5
[25] Schiller A and Herschfield S 2000 *Phys. Rev.* B **62** R16271–4

[26] Lobaskin D and Kehrein S 2005 *Phys. Rev.* B **71** 193303
[27] Shao H, Langreth D C and Nordlander P 1994 *Phys. Rev.* B **49** 13929–47
[28] Wingreen N S and Meir Y 1994 *Phys. Rev.* B **49** 11040
[29] Langreth D C and Nordlander P 1991 *Phys. Rev.* B **43** 2541
[30] Rosch A, Kroha J and Wolfle P 2001 *Phys. Rev. Lett.* **87** 156802
[31] Abrikosov A A 1965 *Physics* **2** 5
[32] Sivan N and Wingreen N S 1996 *Phys. Rev.* B **54** 11622